

Journal of Innovative Optical Health Sciences

GCR-Net: 3D Graph Convolution-based Residual Network for Robust Reconstruction in Cerenkov Luminescence Tomography --Manuscript Draft--

Manuscript Number:	JIOHS-D-22-00067R1
Full Title:	GCR-Net: 3D Graph Convolution-based Residual Network for Robust Reconstruction in Cerenkov Luminescence Tomography
Article Type:	Research Paper
Section/Category:	Special Issue: Celebrating the 15th Anniversary of JIOHS and the 70th Anniversary of HUST
Keywords:	Cerenkov Luminescence Tomography; optical molecular imaging; optical tomography; deep learning; 3D Graph Convolution
Corresponding Author:	Xin Cao Northwest University CHINA
Corresponding Author Secondary Information:	
Corresponding Author's Institution:	Northwest University
Corresponding Author's Secondary Institution:	
First Author:	weitong li
First Author Secondary Information:	
Order of Authors:	weitong li
	mengfei du
	yi chen
	haolin wang
	linzhi su
	huangjian yi
	fengjun zhao
	kang li
	Lin wang
	Xin Cao
Order of Authors Secondary Information:	
Abstract:	<p>Cerenkov Luminescence Tomography (CLT) is a novel and potential imaging modality which can display the three-dimensional distribution of radioactive probes. However, due to the severe ill-posed inverse problem, obtaining accurate reconstruction results is still a challenge for traditional model-based methods. The recently emerged deep learning-based methods can directly learn the mapping relation between the surface photon intensity and the distribution of the radioactive source, which effectively improves the performance of CLT reconstruction. However, the previously proposed deep learning-based methods cannot work well when the order of input is disarranged. In this paper, a novel 3D graph convolution-based residual network, GCR-Net, is proposed, which can obtain a robust and accurate reconstruction result from the photon intensity of the surface. Additionally, it is proved that the network is insensitive to the order of input. The performance of this method was evaluated with numerical simulations and in vivo experiments. The results demonstrated that compared with the existing methods, the proposed method can achieve efficient and accurate reconstruction in localization and shape recovery by utilizing three-dimensional</p>

	information.
Response to Reviewers:	Please see the response letter.

Revised manuscript submitted to Journal of Innovative Optical Health Science

Manuscript ID: JIOHS-D-22-00067

Title: GCR-Net: 3D Graph Convolution-based Residual Network for Robust Reconstruction in Cerenkov Luminescence Tomography

Authors: Weitong Li,^{1,2} Mengfei Du,^{1,2} Yi Chen,^{1,2} Haolin Wang,^{1,2} Linzhi Su,^{1,2,*} Huangjian Yi,¹ Fengjun Zhao,¹ Kang Li,^{1,2} Lin Wang,³ and Xin Cao^{1,2,*}

In response to the reviewers' comments, we have revised the original manuscript as follows:

1. We have tried our best to clarify all the questions raised by the reviewers.
2. We have added the relevant experiments on disarranging the order of input for dual-source simulation.
3. In vivo experiments, we have added more experimental details.
4. We have revised the syntax error as well as the formula error in the manuscript. The error of the title serial number in Section 3.1 has been corrected.
5. We have added the depth information of the source, and indicated the location of sources in Fig. 4, 6, and 7. The cross-sections of (b1), (c1) in Fig. 6 have been modified to maintain a uniform cross-sectional position.

We wish to thank the reviewers and editor for their valuable comments and useful suggestions, which are very helpful for improving this manuscript.

Reply to comments of Reviewer 1:

1. The authors emphasizes that one of the main advantages of GCR-Net is that it is insensitive to the order of input. They also said "the order of input was determined at the discretized process by COMSOL Multiphysics." What does the order of input mean? Please specify the network input and explain how to disarrange the order of input (for the simulation of model3 and model 4). In addition, how about the result if disarrange the order of input for dual-source simulation?

[Reply]

We thank the reviewer for this kind comment. **Firstly**, CLT reconstruction depends on the description of photon propagation. With the application of Finite Element Analysis, the model of light propagation would be transformed into a linear equation. The permissible region of the imaging object is partitioned into n nodes by using FEM software. Each node contains the coordinates and intensity. Thus, the input of the network are the coordinates and the intensity of each node, and the size is $n \times 4$. The order of input means the order of the nodes, which is generated by FEM software automatically. **Secondly**, to disarrange the order of input, the index of each node in the input has been shuffled randomly. **Thirdly**, for dual-source simulation, our network can still work well when the order of input has been disarranged (the result can be found in Table 6). The relevant result has been added to the manuscript.

“Two additional dual-source experiments have also been conducted to prove our network is insensitive to the order of input. Two samples with dual sources, named model7 and model8, were used. The experimental setup was the same as the formal experiments on disarranging the order of input for single-source simulation. The quantitative results are shown in Table 6. It can be seen

from Table 6 that in the dual-source experiment, when the order of input points changes, our network can achieve high accuracy in the reconstruction, while MFCNN still cannot work well.

Table 6. Results of the experiments with disarranged order of input for dual source experiment.

method	model\metrics	LE	Dice	SNR
GCR-Net	model7	0.56	0.52	1.83
	model8	0.58	0.37	1.29
MFCNN	model7	/	0	0
	model8	/	0	0

” (please see page 8, section 3.1.3 in revision)

2. The authors use IVTCG and MFCNN for comparisons in this manuscript. Although MFCNN was developed for CLT in ref. 30, it is unlikely that the MFCNN used for that paper exactly match the ones used by the authors. At least, the inputs for the network are quite different. Therefore, the logical conclusion would be that the authors modified this network to make it suitable for their work. Hence, it is essential that the authors briefly mention how they modified the MFCNN in their implementation.

[Reply]

Thanks for your valuable suggestion. **Firstly**, The MFCNN is a deep learning-based method for CLT reconstruction, which takes the node’s intensity as input. The number of neurons of each layer in MFCNN was equal to the number of nodes in the permissible region. **Secondly**, we took MFCNN as a comparison in our experiment. The aim is to evaluate the performance of our network in terms of localization and morphology recovery, as well as the impact of the order of input points. We did not change the implementation of MFCNN, the input and the network configuration of MFCNN are still the same as literature[1].

[1] Z. Zhang, M. Cai, Y. Gao, X. Shi, X. Zhang, Z. Hu, and J. Tian, A novel Cerenkov luminescence tomography approach using multilayer fully connected neural network. *Phys Med Biol*, 64, 245010 (2019).

3. Generally speaking, the size and variety of the datasets impact the effectiveness of deep learning methods. In the numerical Simulation, only 221 single-source samples with same size and shape were considered, will it affect the generalization performance of the DL model? It would be better to illustrate the characteristic of the trained model, such as the training time, convergence curve, etc.

[Reply]

Thanks for your kind comment. **Firstly**, as the distribution of sources should cover the reconstruction permissible region as much as possible, 221 single-source samples with 1mm diameter were collected in our experiment. **Secondly**, 3000 dual source samples were assembled by selecting and adding the corresponding data of single-source samples., which can improve the stability and the robustness of CLT reconstruction. **Thirdly**, the mean value and the standard deviation provided in Table.3 and Table.5 also prove that our network can obtain accurate results at different source positions. In conclusion, 221 single-source samples are sufficient and will not affect

the generalization performance. As for the characteristic of our trained model, the model has been trained for 150 epochs until the loss converged. The convergence curve of the loss is shown as follows:

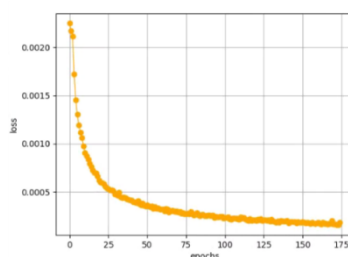


Fig.1 The convergence curve of loss

4. Only a regular phantom model is used in simulation, does it mean that the GCR-Net needs to be retrained for the *in vivo* experiments? How to train a new GCR-Net without any mouse-model data?

[Reply]

We thank the reviewer for this kind comment. **Firstly**, The GCR-Net needs to be retrained for the *in vivo* experiments. Retraining is unavoidable because GCR-Net is trained for a specific imaging object and cannot work well if the imaging object changed. **Secondly**, as a data-driven method, it is impossible to train a new GCR-Net without any mouse-model data. If we want to train a GCR-Net for one mouse model, we need to collect the CT data by using a micro-CT system, and a large amount of optical data can also be generated by using Monte Carlo method, while the generated data can be used for the training of GCR-Net.

5. For the *in vivo* experiments, few details were presented in section 3.2. from the current description, it is not possible to determine whether the author used a homogeneous mode for the *in vivo* experiments. If not, how were the optical parameters for different organs obtained? Please provide more detailed description about the source setting, data acquisition and processing, including the mapping and registration.

[Reply]

Thanks for your valuable comment. We apologized for the lack of details in section 3.2. **Firstly**, for the *in vivo* experiments, a heterogeneous mode was used in the experiment. The optical parameters of each organ are consistent with those in the literature [2]. **Secondly**, in the experiment, a spherical glass vessel with a radius of 1 mm containing about $800 \pm 50 \mu\text{Ci}$ ^{18}F -FDG was used as the artificial Cerenkov luminescence source, which was implanted in the designed location. The stages of *in vivo* experiments include data acquisition and data processing. In the data acquisition, the dual-modality data was collected using a CLT/micro-CT dual-modal system. The mouse was placed on the automatic rotating stage, which was rotating 360 degrees with 1° interval to capture the images of CLI and X-ray projection. The CLI signal with a wavelength of 650nm and white light data were collected using a cooled high-sensitivity EMCCD (-80°C , iXonEM Ultra 888, UK). The CT volume data was acquired by a micro-CT system (tube voltage of 40kV p, tube current of 300mA). After

the data acquisition, data processing was done. First, the trunk sections of the mouse were obtained from the CT data. Then, we segmented the major organs including muscle, lungs, heart, and liver, and then integrated the organs into the mouse model. **Finally**, the CLI images obtained from each angle were mapped and registered to the surface of the mouse torso. The relevant description has been added to the manuscript.

"The experimental data were from the CLT/micro-CT dual-modal system on adult nude mouse.

The mouse was placed on the automatic rotating stage, which was rotating 360 degrees with 1° interval to capture the images of CLI and X-ray projection. The CLI signal with a wavelength of 650nm and white light data were collected using a cooled high-sensitivity EMCCD (-80°C, iXonEM Ultra 888, UK). The CT volume data was acquired by a micro-CT system (tube voltage of 40kV p, tube current of 300mA). The torso section of the mouse is shown in Fig. 7(a). We segmented the main organs of the mouse, including muscle, lung, heart, stomach, liver, and kidney, and integrated these organs into the mouse model. The optical parameters of each organ are consistent with those in the literature 42. A spherical glass vessel with a radius of 1 mm containing about $800 \pm 50 \mu\text{Ci}$ ^{18}F -FDG was used to mimic the lesion containing a radionuclide probe, which was implanted in the designed location. Animal care and protocols were approved by the Fourth Military Medical University Animal Studies Committee. The mouse was used twice for the single-source experiment and dual-source experiment respectively. The position of the source was set at a different place each time. In single-source experiments, the source was implanted into the mouse at a specific location (22, 20, 31.5) mm. In dual-source experiments, the sources were implanted at (20.5, 27.5, 16.5) mm, (14.5, 20, 36) mm respectively. The CLI imaging obtained from each implanted model was mapped and registered to the surface of the mouse torso." (please see page 8, section 3.2 in revision)

[2] H. Yi, D. Chen, W. Li, S. Zhu, X. Wang, J. Liang, and J. Tian, Reconstruction algorithms based on l1-norm and l2-norm for two imaging models of fluorescence molecular tomography: a comparative study, *Journal of Biomedical Optics*, 18, pp. 056013 (2013).

6. The authors claimed that they used a standard mesh (Fig. 2(b). A), but they did not provide any specific information about how to use it. At least, it is necessary to explain the registration between the standard mesh and the actual structure.

[Reply]

We thank the reviewer for this kind comment. **Firstly**, based on Finite Element Analysis, the model of light transmission can be transformed into a linear equation[3]. The mesh data for our phantom was generated by using COMSOL Multiphysics. **Secondly**, in the numerical simulation experiments, Monte Carlo method, which has been widely used to simulate light transmission, was utilized to generate the training data, and the procedure was implemented by using Molecular Optical Simulation Environment (MOSE v2.3). We converted the mesh into the model recognizable by MOSE. **Thirdly**, as the mesh data is generated by using COMSOL Multiphysics according to the phantom's actual structure, the standard mesh and the actual structure are intrinsically registered.

[3] S. Jiang, J. Liu, G. Zhang, Y. An, H. Meng, Y. Gao, K. Wang, and J. Tian, Reconstruction of Fluorescence

Reply to comments of Reviewer 2:

Reviewer #2: CLT is one kind of optical imaging modalities which can display the three-dimensional distribution of radioactive probes. Different from the traditional model-based methods, the author proposed a 3D graph convolution-based neural network for CLT and obtained relatively accurate reconstruction results. The work is interesting and the paper is well written. However, several minor issues should be addressed before publication:

1. A Leaky-Relu layer was used after an EdgeConv layer. Why was the Leaky-Relu chosen as the activation function?

[Reply]

Thanks for your kind comment. Leaky-ReLU is a type of activation function based on ReLU, which has a small slope for negative values instead of a flat slope. Its definition is as follows:

$$\text{LeakyReLU}(x) = \begin{cases} x, & \text{if } x > 0 \\ ax, & \text{if } x < 0 \end{cases}$$

where a is a constant with a small value. Compared with ReLU, Leaky ReLU can solve the problem of ReLU dying. In the DGCNN, the Leaky-ReLU layer was used for the classification task, which has achieved great performance. Also, in our experiments, the network which used Leaky-ReLU layer as activation function works well. Therefore, we chose Leaky Relu as our activation function.

2. On Page 3, the sign of the nonlinear function mentioned in the sentence was inconsistent with that in the formula.

[Reply]

Thanks for your valuable suggestion. We apologized for our mistakes and it has been corrected in the manuscript, which is as follows:

“In the EdgeConv layer, edge feature which describes the relationships between a node and its neighbors is proposed. It is defined as follows:

$$e_{ij} = h_{\theta}(v_i, v_j - v_i) \quad (3)$$

where e_{ij} denotes edge feature. h_{θ} denotes a nonlinear function with a set of learnable parameters.” (please see page 3, section 2.3.1 in revision)

3. It is suggested that the author indicate the position of the light source in Fig. 3,4,6,7.

[Reply]

Thanks for your valuable suggestion. We have indicated the actual position and size of the light source with black circle, which is as follows:

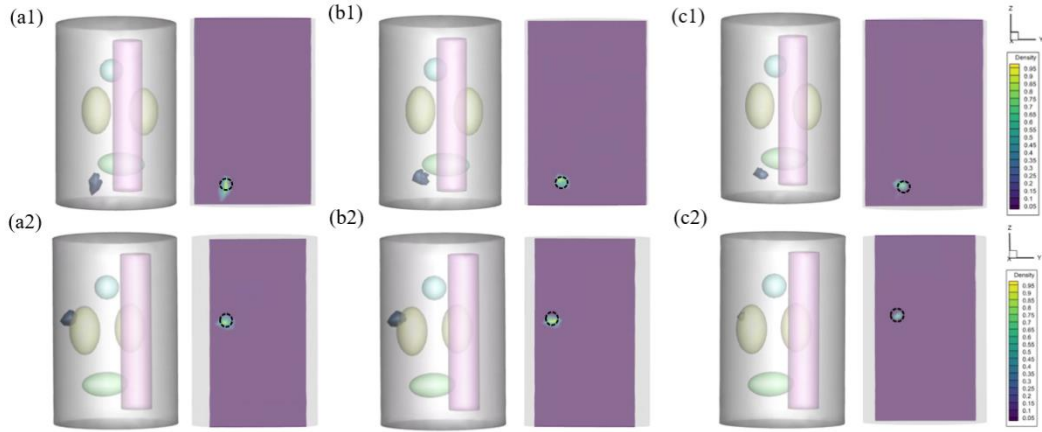


Fig. 4. Comparison results for the single-source experiments. (a1) presents the result reconstructed by GCR-Net method, (b1) and (c1) are the results obtained by the MFCNN method and IVTCG method in model1. (a2), (b2), and (c2) present the results reconstructed by GCR-Net, MFCNN, and IVTCG methods in model2 respectively. The black circle indicates the true position and size of the source.

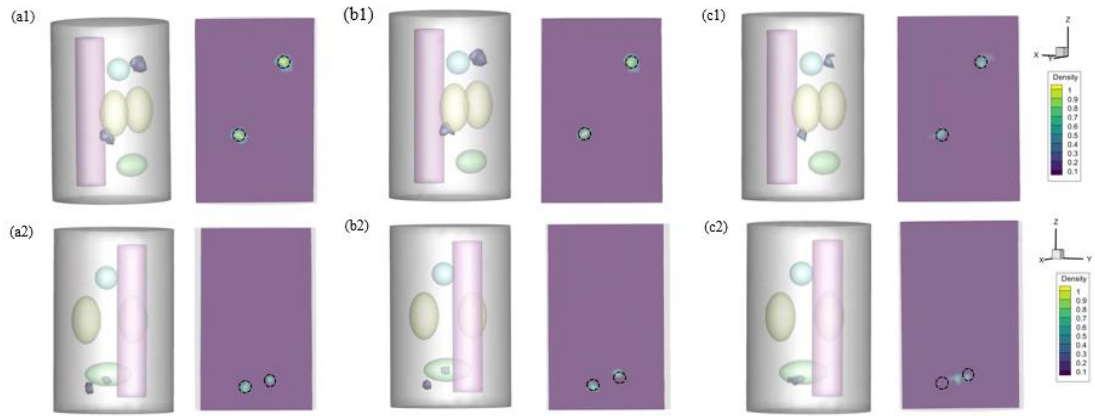


Fig. 6. Comparison results for the dual-source experiments. (a1) presents the result reconstructed by GCR-Net method, (b1) and (c1) are the results obtained by the MFCNN method and IVTCG method in model5. (a2), (b2), and (c2) present the result reconstructed by GCR-Net, MFCNN, and IVTCG methods in model6 respectively. The black circle indicates the true position and size of the source.

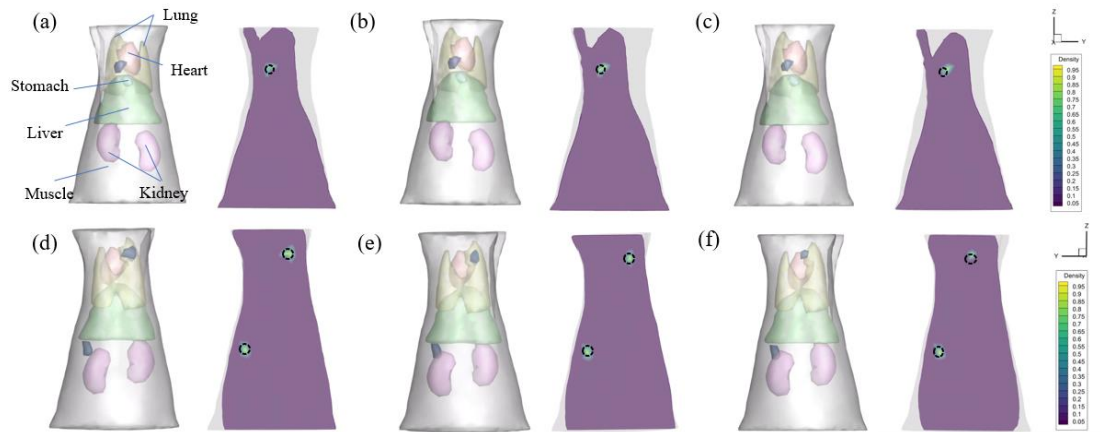


Fig. 7. Comparison results for *in vivo* experiments. (a) presents torso section and the result reconstructed by GCR-Net method, (b) and (c) are the results obtained by the MFCNN method and IVTCG method for the single-source experiment. (d), (e), and (f) present the results reconstructed by GCR-Net, MFCNN, and IVTCG methods for the dual-source experiment. The black circle indicates the true position and size of the source.

(please see pages 7, 8, and 9 in revision respectively)

4. Two samples were used to evaluate the reconstruction in Section 3.3.2, and it is recommended to describe the depth of these two samples. Similarly, please give the depth of the model5 and model6 in Section 3.3.3.

[Reply]

Thanks for your valuable suggestion. We apologized that we did not describe the depth of those samples in the manuscript. The relevant description of depth has been added to the manuscript, which is as follows.

Firstly, in Section 3.3.2, the depth of two samples has been described as follows:

“In model1, the source was set at (-3, -4, 3) mm, while the source in model2 was set at (-6, -5, 17) mm.” (please page 6, section 3.1.2 in revision)

Also, in Section 3.3.3, the depth of two samples has been described as follows:

“In model5, the centers of dual source were set at (-1, 3, 10) mm, (-3, -4, 22) mm respectively. In model6, the sources were set at (-2, -3.5, 4) mm, (-4.5, 0, 5) mm.” (please page 8, section 3.1.2 in revision)

5. In Section 3.2, a radioactive source was implanted into the mouse. The shape and size of the implanted light source should be described.

[Reply]

Thanks for your valuable suggestion. We apologized that we did not describe the shape and size of the implanted light source. We have supplemented the detail of the shape and size of the implanted light source as follows:

“A spherical glass vessel with a radius of 1 mm containing about $800 \pm 50 \mu\text{Ci}$ ^{18}F -FDG was used to mimic the lesion containing a radionuclide probe, which was implanted in the designed location.”

“The position of the source was set at a different place each time. In single-source experiments, the source was implanted into the mouse at a specific location (22, 20, 31.5) mm. In dual-source experiments, the sources were implanted at (20.5, 27.5, 16.5) mm, (14.5, 20, 36) mm respectively.” (please page 9, section 3.2 in revision)

6. For X mentioned in the article, it represents the distribution of real sources in formula (2) and the

distribution of reconstructed sources in formula (6). It is suggested that the author unify related expressions.

[Reply]

Thanks for your valuable suggestion. We apologized for our mistake and it has been corrected in the manuscript, which is as follows:

In formula (6), S_{rec} represents the reconstructed source region and S_{ac} represents the actual source region. It can be defined as:

$$Dice = \frac{2|S_{rec} \cap S_{ac}|}{|S_{rec}| + |S_{ac}|} \quad (6)$$

while in formula (2), X still represents the meaning of the distribution of actual source. (please see page 4, section 2.4 in revision)

GCR-Net: 3D Graph Convolution-based Residual Network for Robust Reconstruction in Cerenkov Luminescence Tomography

Weitong Li,^{1,2} Mengfei Du,^{1,2} Yi Chen,^{1,2} Haolin Wang,^{1,2} Linzhi Su,^{1,2,*} Huangjian Yi,¹ Fengjun Zhao,¹ Kang Li,^{1,2} Lin Wang,³ and Xin Cao^{1,2,*}

¹ School of Information Science and Technology, Northwest University, Xi'an, Shaanxi 710127, China

² National and Local Joint Engineering Research Center for Cultural Heritage Digitization, Xi'an, Shaanxi 710127, China

³ Xi'an University of Technology, Xi'an, Shaanxi 710127, China

*sulinzhi029@163.com, xin_cao@163.com

Abstract: Cerenkov Luminescence Tomography (CLT) is a novel and potential imaging modality which can display the three-dimensional distribution of radioactive probes. However, due to the severe ill-posed inverse problem, obtaining accurate reconstruction results is still a challenge for traditional model-based methods. The recently emerged deep learning-based methods can directly learn the mapping relation between the surface photon intensity and the distribution of the radioactive source, which effectively improves the performance of CLT reconstruction. However, the previously proposed deep learning-based methods cannot work well when the order of input is disarranged. In this paper, a novel 3D graph convolution-based residual network, GCR-Net, is proposed, which can obtain a robust and accurate reconstruction result from the photon intensity of the surface. Additionally, it is proved that the network is insensitive to the order of input. The performance of this method was evaluated with numerical simulations and *in vivo* experiments. The results demonstrated that compared with the existing methods, the proposed method can achieve efficient and accurate reconstruction in localization and shape recovery by utilizing three-dimensional information.

Keywords: Cerenkov Luminescence Tomography; optical molecular imaging; optical tomography; deep learning; 3D Graph Convolution.

1. Introduction

Cerenkov luminescence imaging (CLI) is an optical molecular imaging technology based on Cerenkov radiation, which is electromagnetic radiation emitted when a charged particle travels faster than light in the medium.^{1, 2} Like other optical molecular imaging technologies, CLI has the essential advantage of high sensitivity and low cost. Beyond these advantages, it has wide availability in nuclide probes, which shows its great potential for clinical application.³⁻¹⁵ At present, CLI has been used for tumor imaging, therapy monitoring, etc. However, CLI only performs planar imaging and cannot obtain the three-dimensional distribution of radionuclides, which hinders its further clinical application.

To trace the location and recover the distribution of radionuclides, the tomography method for CLI was proposed and named Cerenkov Luminescence Tomography (CLT).¹⁶ However, the reconstruction of CLT is a highly ill-posed reconstruction problem that makes it difficult to obtain accurate reconstruction results. To improve the reconstruction performance, various model-based methods were proposed for CLT as well as other optical molecular tomography technologies.¹⁷⁻¹⁹ Some researchers used prior information to improve the reconstruction accuracy.²⁰⁻²⁴ For example, Feng et al took permissible region

as prior information and proposed an optimal permissible region selection strategy.²⁵ However, as the prior location of the source cannot be truly obtained, some researchers chose to reconstruct the internal source in the whole region.²⁶⁻³⁰ Zhong et al proposed the whole body reconstruction algorithm along a regularization path.³¹ Besides the strategies mentioned above, taking multispectral information into account was also proposed.^{32, 33} Spinelli et al proposed a multispectral approach that used distinctive information content at the different wavelengths in the reconstruction process, and the result demonstrated that multispectral information can improve the efficiency of CLT.³⁴

The recent success in deep learning demonstrated its great potential in optical imaging tomography. By employing a deep neural network, the mapping relation between the surface photon intensity and internal radioactive source can be learned directly. Zhang et al firstly applied a multilayer fully connected neural network (MFCNN) to reconstruct the distribution of the radioactive source.³⁵ Cao et al proposed a CLT reconstruction framework based on a stacked denoising auto-encoder, in which the residual error was learned between the preliminary reconstruction result and the accurate result.³⁶ Zhang et al applied an attention mechanism-based locally connected network for CLT, which improved the accuracy and stability of CLT reconstruction.³⁷ For the reconstruction in bioluminescence tomography and fluorescence molecular tomography, Meng et al proposed a locally connected network based on the K-Nearest Neighbor method, which achieved accurate morphological FMT reconstruction in a short time.³⁸ Yu et al proposed a one-dimensional convolutional neural network, which significantly reduced the number of parameters.³⁹ The methods mentioned above take the node intensity as the input of the network, and the nodes are generated by finite element method (FEM) software.^{20, 26} However, the trained network is sensitive to the order of input, in other words, even for the same imaging model, if the order of input is disarranged, the trained network cannot work well.

In this paper, a 3D graph convolution-based neural network with a residual architecture for CLT reconstruction, named GCR-Net, is proposed to overcome the shortcomings of existing reconstruction methods based on deep learning. GCR-Net is divided into several residual blocks and each block consists of basic residual units. Firstly, a three-dimensional graph convolution operator is introduced to extract and aggregate features. Secondly, coordinates and the surface photon intensity are performed as the input, which suggests that three-dimensional information is utilized in our network. It is noteworthy that the proposed network does not rely on a specific order for input points because of the characteristic of the three-dimensional graph convolution operator, which means that an accurate result can be obtained even if the order of input is disarranged.

The rest of this paper is structured as follows: In Section II, basic knowledge of CLT reconstruction and the details of GCR-Net are introduced. In Section III, the numerical simulation experiments as well as the *in vivo* studies are illustrated to prove the effectiveness of our network. In Section IV, the discussion and conclusion are illustrated.

2. Methodology

2.1. Model-based CLT Reconstruction

For model-based CLT reconstruction, Radiative Transfer Equation (RTE) is used to mathematically describe the propagation of light in biological tissue.^{40, 41} However, RTE has high computational complexity. To simplify the equation, Diffusion Approximation (DA) model is proposed and widely used.^{16, 42} Based on finite element analysis, a linear relation between the surface photon intensity and the distribution of the radioactive source is established, which can be defined as follows:

$$\Phi = AX \quad (1)$$

where Φ is the photon intensity of the surface. A is the system matrix determined by the characteristics of biological organs. X is the distribution of the radioactive source.

2.2. Deep Learning-based CLT Reconstruction

Deep learning-based CLT reconstruction uses neural network to establish the mapping relation between the photon intensity of surface and the radioactive source directly. Therefore, the deviation between the real photon propagation process and the simplified photon propagation process can be avoided. The deep learning-based method can be described as follows:

$$\min \|f_{nn}(\Phi|\theta) - X\|_2^2 \quad (2)$$

where f_{nn} denotes the reconstruction neural network. θ denotes network weight which is iteratively updated to reduce the error between the reconstructed radioactive source and the actual radioactive source. Φ denotes the surface photon intensity as an input to the network. X denotes the actual distribution of the radioactive source.

2.3. Three-dimensional Graph Convolution-based Residual Network for CLT

Generally speaking, the permissible domain can be discretized into n nodes, which can be generated by finite element method software. Each node has three-dimensional information as well as photon intensity information. However, three-dimensional information has been ignored in the previous deep learning-based methods. Hence, a residual network based on 3D graph convolution for CLT, named GCR-Net, which fully utilizes 3D information is described in detail in this section.

2.3.1. Three-dimensional Graph Convolution

As each node and its neighbors can be organized as graph structure, and inspired by DGCNN,⁴³ the EdgeConv layer is introduced into our network. In the EdgeConv layer, edge feature which describes the relationships between a node and its neighbors is proposed. It is defined as follows:

$$e_{ij} = h_{\theta}(v_i, v_j - v_i) \quad (3)$$

where e_{ij} denotes edge feature. h_{θ} denotes a nonlinear function with a set of learnable parameters. v_i denotes the features of the node. v_j denotes the features of its neighbors. To update the features of the node, an edge feature set of size k is calculated first. Then, an aggregation function such as mean operation is applied to aggregate edge features, which is defined as follows:

$$v'_i = \text{mean}_{j:(i,j) \in \epsilon} e_{ij} \quad (4)$$

where v'_i is the new features of the node. In EdgeConv layer, the features of each node are updated.

To update features, a graph structure is in need. In our network, each node was treated as a vertex in the graph. The input graph was constructed by executing a K-NN search to find the nearest neighbor in 3D coordinate space, and the k was set to 20.

2.3.2. Network Architecture

GCR-Net is based on residual architecture. The basic residual unit in our model is named GCUnit. GCUnit consists of three EdgeConv layers. Each EdgeConv layer is followed by a Leaky-Relu layer. A skip connection is added between the input and the output of GCUnit. As shown in Fig. 1, GCR-Net is composed of 5 residual blocks, named GCBBlock. There are two types of GCBBlock. One consists of two GCUnits and the other consists of three GCUnits. A skip connection is introduced in GCBBlock to reuse a previously learned feature, which connects from the input of GCBBlock to its output. Before entering the first GCBBlock, an EdgeConv layer with 8 output channels is performed, followed by a Leaky-Relu layer. At the end of the last GCBBlock, an EdgeConv layer with 1 output channel is performed and then a Leaky-Relu layer is attached. The network configuration we used is shown in Table 1. Taking GCBBlock 1 as an example, it consists of 2 GCUnits. Each GCUnit consists of three EdgeConv layers with 8, 16, and 16 output channels respectively. It should be noted that, in our network, normalized coordinates and intensity are taken as inputs, and the size is $n \times 4$. The output of GCR-Net is the reconstructed distribution of the radioactive source.

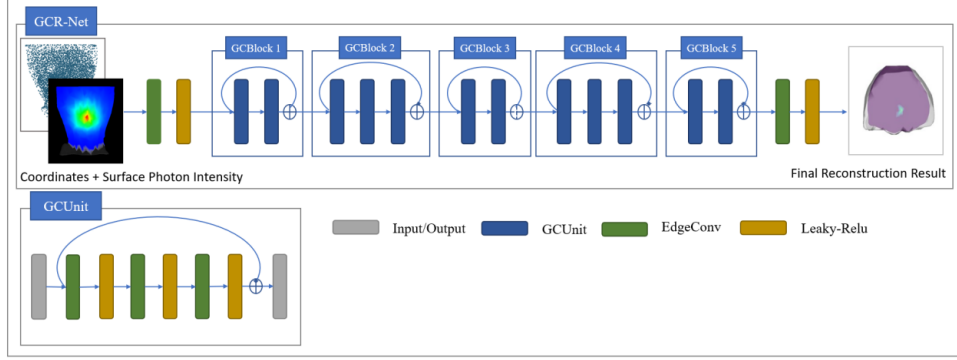


Fig. 1. The network structure of GCR-Net. Coordinates and surface photon intensity are taken as input, and the output is the final reconstruction result.

Table 1. Network configuration

EdgeConv layer	GCBLOCK 1	GCBLOCK 2	GCBLOCK 3	GCBLOCK 4	GCBLOCK 5	EdgeConv layer
[8]	$\begin{bmatrix} 8 \\ 16 \\ 16 \end{bmatrix} * 2$	$\begin{bmatrix} 32 \\ 32 \\ 64 \end{bmatrix} * 3$	$\begin{bmatrix} 64 \\ 64 \\ 128 \end{bmatrix} * 2$	$\begin{bmatrix} 64 \\ 32 \\ 32 \end{bmatrix} * 3$	$\begin{bmatrix} 16 \\ 8 \\ 8 \end{bmatrix} * 2$	[1]

2.4. Implementation Details and Evaluation Metrics

The training and test of GCR-Net were implemented using Pytorch and Python 3.7. All operation was performed on a personal computer with an AMD Ryzen 7 1700 Eight-Core Processor 3.00 GHz CPU and a NVIDIA GeForce GTX 1080 Ti GPU. The optimization function of GCR-Net was Adam optimizer with a learning rate of 0.001. Mean Square Error (MSE) Loss was adopted as a loss function.

The performance of GCR-Net was quantitatively evaluated with the following three metrics: location error (LE), Dice coefficient, and signal-to-noise ratio (SNR).

Location error is defined as the position error between the reconstructed radioactive source and the actual radioactive source. L_r represents the barycenter of the reconstructed radioactive source and L_0 represents the barycenter of the actual radioactive source. It can be defined as:

$$LE = \|L_r - L_0\|_2 \quad (5)$$

Dice coefficient is used to evaluate the similarity between the reconstructed source region and the actual source region. S_{rec} represents the reconstructed source region and S_{ac} represents the actual source region. It can be defined as:

$$Dice = \frac{2|S_{rec} \cap S_{ac}|}{|S_{rec}| + |S_{ac}|} \quad (6)$$

The signal-to-noise ratio (SNR) is used to measure the visual quality. u'_i represents the energy of the i^{th} node in the reconstruction result, u^i represents the energy of the i^{th} node in the original numerical model. n is the total number of nodes in the numerical model. It can be defined as:

$$SNR = \frac{\sum_{i=1}^n u_i^2}{\sum_{i=1}^n (u_i - u'_i)^2} \quad (7)$$

3. Experiments and Results

In this section, the performance of GCR-Net was evaluated by performing numerical simulations and *in vivo* experiments. IVTCG and MFCNN methods were used as baselines

because they represent one of the most commonly used reconstruction methods in model-based methods and deep learning-based methods respectively.^{35, 37} This section is structured as follows: The first part shows the reconstruction performance of our network in numerical simulation. It contains three experiments, including single-source experiments, dual-source experiments, and experiments of testing the influence of the order of input. The second part presents the reconstruction ability of our method in *in vivo* experiments.

3.1. Numerical Simulation Experiments

3.1.1. Data Collection

A heterogeneous cylindrical phantom with a 10mm diameter and a 30mm height was designed to simulate the mouse body. The phantom consists of five kinds of organs: heart, lungs, bone, liver, and muscle. The phantom is exhibited in Fig. 2. Optical parameters of all organs are presented in Table 2, which were obtained from literature⁴⁴.

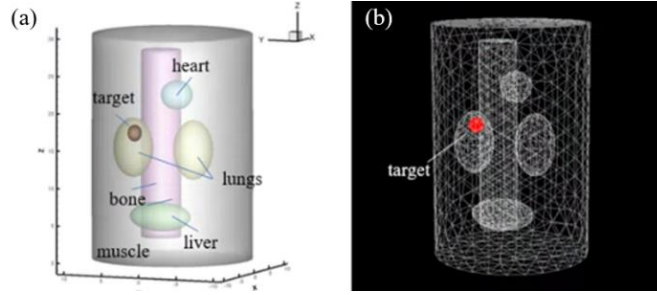


Fig. 2. The numerical phantom. (a) shows a single-source phantom, and (b) shows the standard mesh

Table 2. Optical parameters of different organs.

Component	Absorption coefficient μ_a	Scattering coefficient μ_s
Muscle	0.016	0.510
Heart	0.011	1.053
Lungs	0.036	2.246
Liver	0.012	2.472
Bone	0.021	2.864

The numerical phantom was discretized into a standard mesh with 4626 nodes by using COMSOL Multiphysics V5.6 (COMSOL Inc., USA) software, from which its coordinates can be obtained.⁴⁵ The order of input was determined at the discretized process by COMSOL Multiphysics. The standard mesh is exhibited in Fig. 2(b). A small spherical radioactive source with 1mm diameter was set in the model to present the tumor. The photon wavelength was set to 650nm to ensure appropriate penetration. As a data-driven method, plenty of data is in need for training. As it is difficult to collect a large amount of data from *in vivo* experiments, Monte Carlo method was used for data collection, because it can simulate the transmission process of photons. All the Monte Carlo simulation was conducted using Molecular Optical Simulation Environment (MOSE 2.3).⁴⁶ We simulated a total of 221 single-source samples to make the radioactive source cover the permissible region as much as possible. 3000 dual-source samples were assembled by randomly selecting and adding the corresponding data of two single-source samples, which were as follows:

$$\Phi_{dual} = \sum_{i \in S_n} \Phi_i \quad (8)$$

$$X_{dual} = \sum_{i \in S_n} X_i \quad (9)$$

where Φ_{dual} represents the surface photon of the assembled sample, Φ_i represents the surface photon of the i^{th} single-source sample. X_{dual} and X_i represent the distribution of the internal source of the assembled sample and the i^{th} single-source sample respectively. S_n is the set of single-source samples.

Overall, in this paper, 221 single-source samples and 3000 assembled dual-source samples have been simulated. 80% of the dataset was randomly selected for training and the others were selected for testing.

3.1.2. Single-source Simulation Result

To quantitatively analyze the effect of our network for single-source simulation, the mean value and deviation of different evaluation indexes were calculated, as exhibited in Table 3. As suggested from Table 3, GCR-Net obtained the lowest mean location error, highest mean Dice, and highest mean SNR. It demonstrated that the proposed network stably improved the accuracy in localization and morphology recovery. Furthermore, the network obtained the minimum LE value of 0.11 and the maximum dice value of 0.79 in some cases, which further proved its advantages in terms of localization capability and morphology recovery ability.

Table 3. Quantitative comparison of single-source simulation (mean \pm SD).

method	LE	Dice	SNR
GCR-Net	0.43 \pm 0.22	0.51 \pm 0.11	1.97 \pm 0.41
MFCNN	0.52 \pm 0.23	0.38 \pm 0.12	1.49 \pm 0.46
IVTCG	0.76 \pm 0.27	0.34 \pm 0.15	1.32 \pm 0.55

Two samples, named model1 and model2, were used to measure the single-source reconstruction result of different methods. In model1, the source was set at (-3, -4, 3) mm, while the source in model2 was set at (-6, -5, 17) mm. The quantitative results are exhibited in Fig. 3, which show that our network still performs better in LE, Dice, and SNR. Fig. 4 shows the 3D visualization as well as the 2D cross sections of reconstruction results obtained by GCR-Net, MFCNN, and IVTCG respectively.

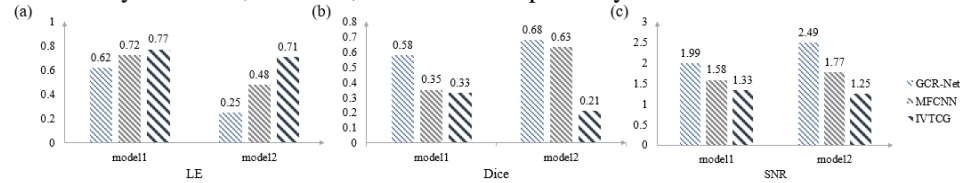


Fig. 3. The quantitative results of selected single-source samples. (a), (b), and (c) shows the quantitative value of LE, Dice, and SNR respectively.

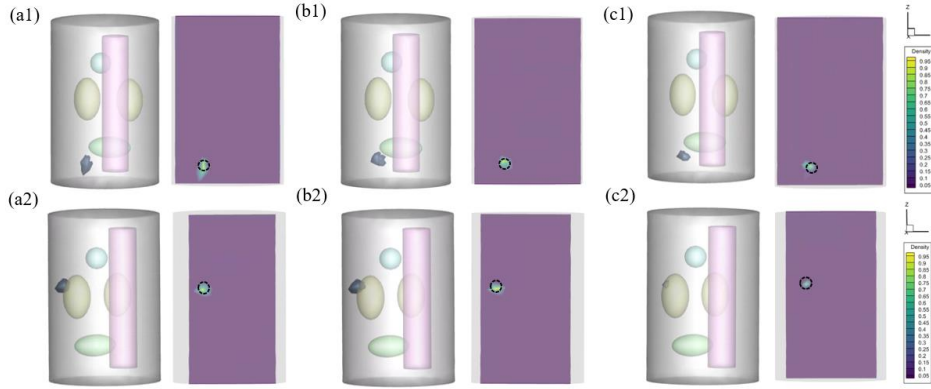


Fig. 4. Comparison results for the single-source experiments. (a1) presents the result reconstructed by GCR-Net method, (b1) and (c1) are the results obtained by the MFCNN method and IVTCG method in model1. (a2), (b2), and (c2) present the results reconstructed by GCR-Net, MFCNN, and IVTCG methods in model2 respectively. The black circle indicates the true position and size of the source.

Two additional single-source experiments have been conducted to prove our network is insensitive to the order of input. Two samples with single source, named model3 and model4, were used. In this experiment, the order of input has been disarranged. MFCNN was performed as a comparative experiment under the same conditions. It is noteworthy that the previously trained network was directly used without further training. The quantitative results are exhibited in Table 4. It can be demonstrated from Table 4 that MFCNN is sensitive to the input order. If the order of input is disarranged, the MFCNN cannot work well. On the contrary, GCR-Net can successfully reconstruct the distribution of the radioactive source with high accuracy in all experiments.

Table 4. Results of the experiments with disarranged order of input for single source.

method	model\metrics	LE	Dice	SNR
GCR-Net	model3	0.72	0.54	1.99
	model4	0.76	0.34	1.25
MFCNN	model3	/	0	0
	model4	/	0	0

3.1.3. Dual-source Simulation Result

Dual-source simulation experiments were carried out to further evaluate the performance of our methods on multi-source simulation. The quantitative results are exhibited in Table 5. The results in Table 5 revealed that our method still had its superiority in LE, Dice, and SNR, which presented a promising performance of reconstruction. However, compared with the single-source samples, the results of the dual-source samples were worse, which was probably caused by the raise in reconstruction complexity.

Table 5. Quantitative comparison of dual-source simulation (mean \pm SD).

method	LE	Dice	SNR
GCR-Net	0.69 \pm 0.25	0.37 \pm 0.10	1.68 \pm 0.45
MFCNN	0.75 \pm 0.28	0.31 \pm 0.11	1.29 \pm 0.47
IVTCG	0.91 \pm 0.33	0.16 \pm 0.11	1.04 \pm 0.50

Two samples, named model5 and model6, were used to measure the dual-source reconstruction result of different methods. In model5, the centers of dual source were set at (-1, 3, 10) mm, (-3, -4, 22) mm respectively. In model6, the sources were set at (-2, -3.5, 4) mm, (-4.5, 0, 5) mm. The quantitative results are exhibited in Fig. 5, which illustrate a consistent trend with the former experiments. Fig. 6 illustrates the visualization of the dual-source reconstruction results and suggests that both reconstructed radioactive sources have a clear shape and are easy to distinguish.

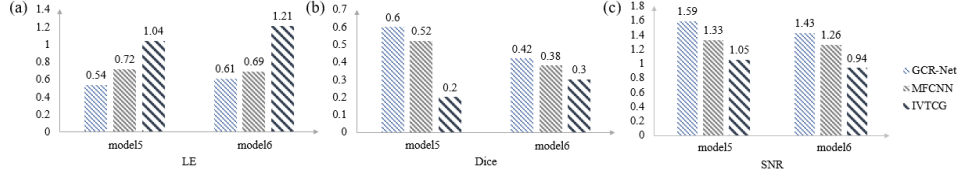


Fig. 5. The quantitative results of selected dual-source samples. (a), (b), and (c) shows the quantitative value of LE, Dice, and SNR respectively.

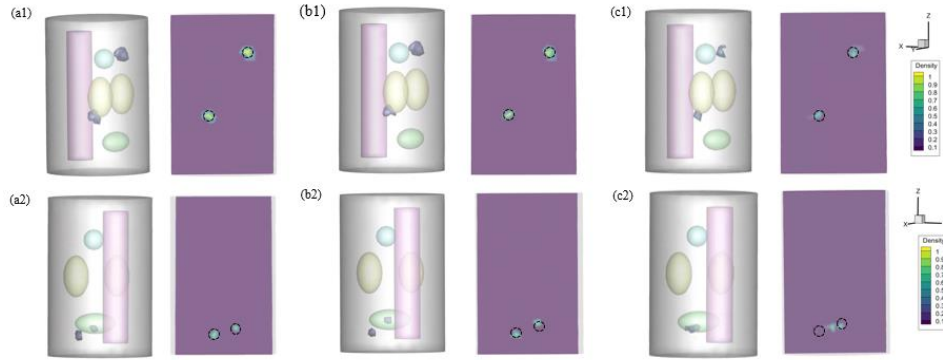


Fig. 6. Comparison results for the dual-source experiments. (a1) presents the result reconstructed by GCR-Net method, (b1) and (c1) are the results obtained by the MFCNN method and IVTCG method in model5. (a2), (b2), and (c2) present the result reconstructed by GCR-Net, MFCNN, and IVTCG methods in model6 respectively. The black circle indicates the true position and size of the source.

Two additional dual-source experiments have also been conducted to prove our network is insensitive to the order of input. Two samples with dual source, named model7 and model8, were used. The experimental setup was the same as the formal experiments on disarranging the order of input for single-source simulation. The quantitative results are shown in Table 6. It can be seen from Table 6 that in the dual-source experiment, when the order of input points changes, our network can achieve high accuracy in the reconstruction, while MFCNN still cannot work well.

Table 6. Results of the experiments with disarranged order of input for dual-source experiment.

method	model/metrics	LE	Dice	SNR
GCR-Net	model7	0.56	0.52	1.83
	model8	0.58	0.37	1.29
MFCNN	model7	/	0	0
	model8	/	0	0

3.2. In vivo CLT Reconstruction

The performance of our method was further evaluated with implanted small animal experimental data. The experimental data were from the CLT/micro-CT dual-modal system

on adult nude mouse. The mouse was placed on the automatic rotating stage, which was rotating 360 degrees with 1° interval to capture the images of CLI and X-ray projection. The CLI signal with wavelength of 650nm and white light data were collected using a cooled high-sensitivity EMCCD (-80°C, iXonEM Ultra 888, UK). The CT volume data was acquired by a micro-CT system (tube voltage of 40kV p, tube current of 300mA). The torso section of the mouse is shown in Fig. 7(a). We segmented the main organs of the mouse, including muscle, lung, heart, stomach, liver, and kidney, and integrated these organs into the mouse model. The optical parameters of each organ are consistent with those in the literature⁴⁷. A spherical glass vessel with a radius of 1 mm containing about $800 \pm 50 \mu\text{Ci}$ ^{18}F -FDG was used to mimic the lesion containing a radionuclide probe, which was implanted in the designed location. Animal care and protocols were approved by the Fourth Military Medical University Animal Studies Committee. The mouse was used twice for the single-source experiment and dual-source experiment respectively. The position of the source was set at a different place each time. In single-source experiments, the source was implanted into the mouse at a specific location (22, 20, 31.5) mm. In dual-source experiments, the sources were implanted at (20.5, 27.5, 16.5) mm, (14.5, 20, 36) mm respectively. The CLI imaging obtained from each implanted model was mapped and registered to the surface of the mouse torso. GCR-Net, MFCNN, and IVTCG methods were used to carry out the single-source experiment and dual-source experiment. The results are shown in Table 7 and Fig. 7, which prove the superiority of our network in CLT reconstruction for *in vivo* experiments.

Table 7. Quantitative results for *in vivo* experiments.

method	single-source experiment			dual-source experiment		
	LE	Dice	SNR	LE	Dice	SNR
GCR-Net	0.37	0.81	1.76	0.54	0.87	1.89
MFCNN	0.47	0.66	1.23	0.72	0.69	1.46
IVTCG	0.48	0.65	1.14	0.96	0.50	1.01

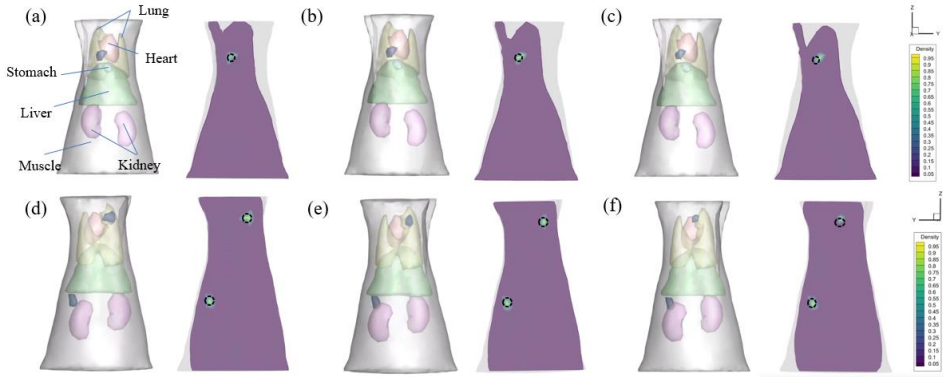


Fig. 7. Comparison results for *in vivo* experiments. (a) presents torso section and the result reconstructed by GCR-Net method, (b) and (c) are the results obtained by the MFCNN method and IVTCG method for the single-source experiment. (d), (e), and (f) present the results reconstructed by GCR-Net, MFCNN, and IVTCG methods for the dual-source experiment. The black circle indicates the true position and size of the source.

4. Discussion and Conclusion

In this paper, a novel GCR-Net was proposed to achieve the accurate reconstruction of CLT. GCR-Net was built by stacking residual blocks based on 3D graph convolution. The main advantages of our network are summarized as follows: firstly, our network fully

utilizes three-dimensional information and improves the performance of CLT reconstruction. Secondly, our network is insensitive to the order of input, which is not able to be satisfied by the traditional fully connected network.

To verify the performance of GCR-Net, single-source and dual-source numerical simulations were implemented. IVTCG method and MFCNN method were adopted for comparison. Quantitative analysis demonstrated that GCR-Net showed a better performance in source localization and morphology recovery. To further evaluate the practicability of GCR-Net, *in vivo* experiments were performed. Consistent with our numerical simulation experiments, GCR-Net obtained the most accurate reconstruction results of radioactive probe distribution in biological tissue.

It is worth noting that our network is insensitive to the order of input. Our method can achieve accurate reconstruction results even if the order is disarranged. It can be explained by the characteristic of the EdgeConv layer. The EdgeConv layer is designed to be invariant to the ordering of neighbors. In EdgeConv layer, the applied aggregation function is a symmetric function. Thus, the output of EdgeConv layer is invariant to the permutation of the input.

However, there are still some limitations of GCR-Net. When calculating edge feature set, the memory cost will be significantly increased with a higher setting of k in KNN method. Besides, the utilization of standard mesh depends on certain software and the registration between standard mesh and actual structure probably brings extra error in CLT reconstruction.

In conclusion, GCR-Net is proposed for CLT reconstruction. It is based on 3D graph convolution and has the advantage of being insensitive to the order of input, which can achieve accurate reconstruction in source localization and morphology recovery. We hope our network can assist CLT reconstruction efficiently.

Acknowledgments

This work was supported by the National Natural Science Foundation of China (61701403,61806164); China Postdoctoral Science Foundation (2018M643719); Young Talent Support Program of the Shaanxi Association for Science and Technology (20190107); Key R&D Projects in Qinghai Province (2020-SF-143).

Conflicts of Interest

The authors declare that there are no conflicts of interest related to this article.

References

1. R. Robertson, M. S. Germanos, C. Li, G. S. Mitchell, S. R. Cherry, and M. D. Silva, Optical imaging of Cerenkov light generation from positron-emitting radiotracers. *Phys Med Biol*, 54, N355-65 (2009).
2. C. Qin, J. Zhong, Z. Hu, X. Yang, and J. Tian, Recent Advances in Cerenkov Luminescence and Tomography Imaging. *IEEE Journal of Selected Topics in Quantum Electronics*, 18, 1084-1093 (2012).
3. J. C. Park, G. Il An, S. I. Park, J. Oh, H. J. Kim, Y. Su Ha, E. K. Wang, K. Min Kim, J. Y. Kim, J. Lee, M. J. Welch, and J. Yoo, Luminescence imaging using radionuclides: a potential application in molecular imaging. *Nucl Med Biol*, 38, 321-9 (2011).
4. A. E. Spinelli and F. Boschi, Novel biomedical applications of Cerenkov radiation and radioluminescence imaging. *Phys Med*, 31, 120-9 (2015).

5. T. Song, X. Liu, Y. Qu, H. Liu, C. Bao, C. Leng, Z. Hu, K. Wang, and J. Tian, A Novel Endoscopic Cerenkov Luminescence Imaging System for Intraoperative Surgical Navigation. *Mol Imaging*, 14, 443-9 (2015).
6. J. Axelsson and J. Krohn, Cerenkov Luminescence Imaging for Accurate Placement of Radioactive Plaques in Episcleral Brachytherapy of Intraocular Tumors. *Invest Ophthalmol Vis Sci*, 56, 7362-8 (2015).
7. Z. Hu, Y. Qu, K. Wang, X. Zhang, J. Zha, T. Song, C. Bao, H. Liu, Z. Wang, J. Wang, Z. Liu, H. Liu, and J. Tian, In vivo nanoparticle-mediated radiopharmaceutical-excited fluorescence molecular imaging. *Nat Commun*, 6, 7560 (2015).
8. Z. Zhang, M. Cai, C. Bao, Z. Hu, and J. Tian, Endoscopic Cerenkov luminescence imaging and image-guided tumor resection on hepatocellular carcinoma-bearing mouse models. *Nanomedicine*, 17, 62-70 (2019).
9. Y. Xu, E. Chang, H. Liu, H. Jiang, S. S. Gambhir, and Z. Cheng, Proof-of-concept study of monitoring cancer drug therapy with cerenkov luminescence imaging. *J Nucl Med*, 53, 312-317 (2012).
10. D. L. Thorek, A. Ogirala, B. J. Beattie, and J. Grimm, Quantitative imaging of disease signatures through radioactive decay signal conversion. *Nat Med*, 19, 1345-50 (2013).
11. X. Cao, Y. Zhan, X. Cao, J. Liang, and X. Chen, Harnessing the Power of Cerenkov Luminescence Imaging for Gastroenterology: Cerenkov Luminescence Endoscopy. *Current Medical Imaging Reviews*, 13, 50-57 (2017).
12. X. Cao, X. Chen, F. Kang, Y. Lin, M. Liu, H. Hu, Y. Nie, K. Wu, J. Wang, J. Liang, and J. Tian, Performance evaluation of endoscopic Cerenkov luminescence imaging system: in vitro and pseudotumor studies. *Biomed Opt Express*, 5, 3660-70 (2014).
13. D. Fan, X. Zhang, L. Zhong, X. Liu, Y. Sun, H. Zhao, B. Jia, Z. Liu, Z. Zhu, J. Shi, and F. Wang, (68)Ga-labeled 3PRGD2 for dual PET and Cerenkov luminescence imaging of orthotopic human glioblastoma. *Bioconjug Chem*, 26, 1054-60 (2015).
14. X. Cao, X. Chen, F. Kang, X. Cao, Y. Zhan, J. Wang, K. Wu, and J. Liang, Sensitivity improvement of Cerenkov luminescence endoscope with terbium doped Gd₂O₂S nanoparticles. *Applied Physics Letters*, 106, 4 (2015).
15. H. Chen, K. Shou, S. Chen, C. Qu, Z. Wang, L. Jiang, M. Zhu, B. Ding, K. Qian, and A. Ji, Smart Self- Assembly Amphiphilic Cyclopeptide-Dye for Near- Infrared Window- II Imaging. *Advanced Materials*, 33, 2006902 (2021).
16. C. Li, G. S. Mitchell and S. R. Cherry, Cerenkov luminescence tomography for small-animal imaging. *Opt Lett*, 35, 1109-11 (2010).
17. Q. Zhang, H. Zhao, D. Chen, X. Qu, X. Chen, X. He, W. Li, Z. Hu, J. Liu, J. Liang, and J. Tian, Source sparsity based primal-dual interior-point method for three-dimensional bioluminescence tomography. *Optics Communications*, 284, 5871-5876 (2011).
18. H. Guo, Z. Hu, X. He, X. Zhang, M. Liu, Z. Zhang, X. Shi, S. Zheng, and J. Tian, Non-convex sparse regularization approach framework for high multiple-source resolution in cerenkov luminescence tomography. *Optics Express*, 25, 28068-28085 (2017).

19. H. Guo, J. Yu, Z. Hu, H. Yi, Y. Hou, and X. He, A hybrid clustering algorithm for multiple-source resolving in bioluminescence tomography. *J Biophotonics*, 11, e201700056 (2018).
20. W. Cong, G. Wang, D. Kumar, Y. Liu, M. Jiang, L. Wang, E. Hoffman, G. McLennan, P. McCray, J. Zabner, and A. Cong, Practical reconstruction method for bioluminescence tomography. *Opt Express*, 13, 6756-71 (2005).
21. M. A. Naser and M. S. Patterson, Bioluminescence tomography using eigenvectors expansion and iterative solution for the optimized permissible source region. *Biomed Opt Express*, 2, 3179-93 (2011).
22. M. A. Naser and M. S. Patterson, Improved bioluminescence and fluorescence reconstruction algorithms using diffuse optical tomography, normalized data, and optimized selection of the permissible source region. *Biomed Opt Express*, 2, 169-84 (2010).
23. J. Liu, Y. Wang, X. Qu, X. Li, X. Ma, R. Han, Z. Hu, X. Chen, D. Sun, R. Zhang, D. Chen, D. Chen, X. Chen, J. Liang, F. Cao, and J. Tian, In vivo quantitative bioluminescence tomography using heterogeneous and homogeneous mouse models. *Opt Express*, 18, 13102-13 (2010).
24. C. Qin, S. Zhu, J. Feng, J. Zhong, X. Ma, P. Wu, and J. Tian, Comparison of permissible source region and multispectral data using efficient bioluminescence tomography method. *Journal of biophotonics*, 4, 824-839 (2011).
25. J. Feng, K. Jia, G. Yan, S. Zhu, C. Qin, Y. Lv, and J. Tian, An optimal permissible source region strategy for multispectral bioluminescence tomography. *Opt Express*, 16, 15640-54 (2008).
26. Z. Hu, X. Chen, J. Liang, X. Qu, D. Chen, W. Yang, J. Wang, F. Cao, and J. Tian, Single photon emission computed tomography-guided Cerenkov luminescence tomography. *Journal of Applied Physics*, 112, (2012).
27. K. Liu, Y. Lu, J. Tian, C. Qin, X. Yang, S. Zhu, X. Yang, Q. Gao, and D. Han, Evaluation of the simplified spherical harmonics approximation in bioluminescence tomography through heterogeneous mouse models. *Opt Express*, 18, 20988-1002 (2010).
28. J. Dutta, S. Ahn, C. Li, S. R. Cherry, and R. M. Leahy, Joint L1 and total variation regularization for fluorescence molecular tomography. *Physics in Medicine & Biology*, 57, 1459 (2012).
29. K. Liu, J. Tian, C. Qin, X. Yang, D. Han, P. Wu, and S. Zhu, Tomographic bioluminescence imaging reconstruction via a dynamically sparse regularized global method in mouse models. *Journal of biomedical optics*, 16, 046016 (2011).
30. M. Cai, Z. Zhang, X. Shi, J. Yang, Z. Hu, and J. Tian, Non-negative Iterative Convex Refinement Approach for Accurate and Robust Reconstruction in Cerenkov Luminescence Tomography. *IEEE Trans Med Imaging*, (2020).
31. J. Zhong, J. Tian, X. Yang, and C. Qin, Whole-body Cerenkov luminescence tomography with the finite element SP(3) method. *Ann Biomed Eng*, 39, 1728-35 (2011).
32. Z. Hu, X. Ma, X. Qu, W. Yang, J. Liang, J. Wang, and J. Tian, Three-dimensional noninvasive monitoring iodine-131 uptake in the thyroid

- using a modified Cerenkov luminescence tomography approach. *PLoS One*, 7, e37623 (2012).
33. H. Liu, X. Yang, T. Song, C. Bao, L. Shi, Z. Hu, K. Wang, and J. Tian, Multispectral hybrid Cerenkov luminescence tomography based on the finite element SPn method. *J Biomed Opt*, 20, 86007 (2015).
34. A. E. Spinelli, C. Kuo, B. W. Rice, R. Calandrino, P. Marzola, A. Sbarbati, and F. Boschi, Multispectral Cerenkov luminescence tomography for small animal optical imaging. *Opt Express*, 19, 12605-18 (2011).
35. Z. Zhang, M. Cai, Y. Gao, X. Shi, X. Zhang, Z. Hu, and J. Tian, A novel Cerenkov luminescence tomography approach using multilayer fully connected neural network. *Phys Med Biol*, 64, 245010 (2019).
36. X. Cao, X. Wei, F. Yan, L. Wang, L. Su, Y. Hou, G. Geng, and X. He, A Novel Stacked Denoising Autoencoder-Based Reconstruction Framework for Cerenkov Luminescence Tomography. *IEEE Access*, 7, 85178-85189 (2019).
37. X. Zhang, M. Cai, L. Guo, Z. Zhang, B. Shen, X. Zhang, Z. Hu, and J. Tian, Attention mechanism-based locally connected network for accurate and stable reconstruction in Cerenkov luminescence tomography. *Biomedical Optics Express*, 12, 7703-7716 (2021).
38. H. Meng, Y. Gao, X. Yang, K. Wang, and J. Tian, K-nearest Neighbor Based Locally Connected Network for Fast Morphological Reconstruction in Fluorescence Molecular Tomography. *IEEE Trans Med Imaging*, (2020).
39. J. Yu, C. Dai, X. He, H. Guo, S. Sun, and Y. Liu, Bioluminescence Tomography Based on One-Dimensional Convolutional Neural Networks. *Frontiers in Oncology*, 4182 (2021).
40. A. D. Klose, The forward and inverse problem in tissue optics based on the radiative transfer equation: a brief review. *J Quant Spectrosc Radiat Transf*, 111, 1852-1853 (2010).
41. W. Cai, M. Xu and R. Alfano, Three-dimensional radiative transfer tomography for turbid media. *IEEE Journal of Selected Topics in Quantum Electronics*, 9, 189-198 (2003).
42. C. Qin, J. Feng, S. Zhu, X. Ma, J. Zhong, P. Wu, Z. Jin, and J. Tian, Recent advances in bioluminescence tomography: methodology and system as well as application. *Laser & Photonics Reviews*, 8, 94-114 (2014).
43. Y. Wang, Y. Sun, Z. Liu, S. E. Sarma, M. M. Bronstein, and J. M. Solomon, Dynamic graph cnn for learning on point clouds. *Acm Transactions On Graphics (tog)*, 38, 1-12 (2019).
44. X. Cao, J. Zhang, J. Yang, C. Fan, F. Zhao, W. Zhou, L. Wang, G. Geng, M. Zhou, and X. Chen, A deep unsupervised clustering-based post-processing framework for high-fidelity Cerenkov luminescence tomography. *Journal of Applied Physics*, 128, 193104 (2020).
45. B. Parvitte, C. Risser, R. Vallon, and V. Zéninari, Quantitative simulation of photoacoustic signals using finite element modelling software. *Applied Physics B*, 111, 383-389 (2013).
46. S. Ren, X. Chen, H. Wang, X. Qu, G. Wang, J. Liang, and J. Tian, Molecular Optical Simulation Environment (MOSE): a platform for the

1
2
3
4
5
6
7
8
9
10
11
12
13
14
15
16
17
18
19
20
21
22
23
24
25
26
27
28
29
30
31
32
33
34
35
36
37
38
39
40
41
42
43
44
45
46
47
48
49
50
51
52
53
54
55
56
57
58
59
60
61
62
63
64
65

simulation of light propagation in turbid media. *PLoS One*, 8, e61304 (2013).

47. H. Yi, D. Chen, W. Li, S. Zhu, X. Wang, J. Liang, and J. Tian, Reconstruction algorithms based on l1-norm and l2-norm for two imaging models of fluorescence molecular tomography: a comparative study. *J Biomed Opt*, 18, 56013 (2013).